Supplement of Atmos. Chem. Phys., 25, 4907–4928, 2025
https://doi.org/10.5194/acp-25-4907-2025-supplement

Atmospheric Chemistry and Physics
Open Access
EGU

Supplement of

Measurement report: Wintertime aerosol characterization at an urban traffic site in Helsinki, Finland

Kimmo Teinilä et al.

Correspondence to: Kimmo Teinilä (kimmo.teinila@fmi.fi)

SUPPLEMENT

Table S1. List showing which compounds were analysed from each sample types and which detector was use.

	Canister Samples	In situ Samples	Tube Samples		Canister Samples	In situ Samples	Tube Samples
Ethane	FID			4-Ethyltoluene		MS	MS
Ethene	FID			1,3,5-Trimethylbenzene		MS	MS
Propane	FID			2-Ethyltoluene		MS	MS
Propene	FID			1,2,4-Trimethylbenzene		MS	MS
2-Methylpropane	FID			1,2,3-Trimethylbenzene		MS	MS
Butane	FID			Hexane		MS	MS
Ethyne	FID			Heptane		MS	MS
T-but-2-ene	FID			Octane		MS	MS
But-1-ene	FID			Nonane		MS	MS
Cis-but-2-ene	FID			Decane		MS	MS
2-Methylbutane	FID			Undecane		MS	MS
n-pentane	FID			Dodecane		MS	MS
1,3-butadiene	FID			Tridecane		MS	MS
T-pent-2-ene	FID			Tetradecane		MS	MS
Pent-1-ene	FID			Pentadecane		MS	MS
Isoprene	FID			Furfural		MS	MS
α-pinene		MS	MS	Benzyl alcohol		MS	MS
Camphene		MS	MS	1,3-Diethylbenzene		MS	MS
Myrcene		MS	MS	o-cresol		MS	MS
β-pinene		MS	MS	1,4-Diethylbenzene		MS	MS
Carene		MS	MS	2-Propyltoluene		MS	MS
p-Cymene		MS	MS	p-cresol		MS	MS
Limonene		MS	MS	2-Ethyl-p-xylene		MS	MS
1,8-Cineol		MS	MS	1,2,4,5-Tetramethylbenzene		MS	MS
Terpinolene		MS	MS	1,3,5-Triethylbenzene		MS	MS
β-caryophyllene		MS	MS	1,4-Dibutylbenzene		MS	MS
Benzene		MS	MS	Naphthalene		MS	MS
Tetrachloromethane		MS	MS	Acenaphthylene		MS	MS
Toluene		MS	MS	Acenaphthene		MS	MS
Ethylbenzene		MS	MS	Fluorene		MS	MS
p/m-xylene		MS	MS	Anthracene		MS	MS
Styrene		MS	MS	Phenanthrene		MS	MS
o-xylene		MS	MS	Fluoranthene		MS	MS
Propylbenzene		MS	MS	Pyrene		MS	MS
3-Ethyltoluene		MS	MS				

Table S2. Instruments at the Traffic Supersite.

Traffic Supersite	
Quantity	Instrument
Chemical composition of aerosol particles	Soot Particle Aerosol Mass Spectrometer (SP-AMS, Aerodyne Research Inc.)
Chemical composition of particulate matter	Aerosol Chemical Speciation Monitor (ACSM, Aerodyne Research Inc.)
Volatile organic compounds (VOCs) and intermediate volatile organic compounds (IVOCs)	In situ thermal desorption-gas chromatograph-mass spectrometer (TD-GC-MS)
Gaseous sulfuric acid	Nitrate based chemical-ionization atmospheric-pressure-interface time-of-flight mass spectrometer (nitrate CI-API-TOF-MS, Aerodyne Research Inc.)
Mobility distribution of ions (0.8–40 nm) and size distribution of particles (2–40 nm)	Neutral cluster and Air Ion Spectrometer (Airel Ltd)
Concentration of SO_2	Enhanced Trace Level SO_2 Analyser (Thermo Scientific™, Model 43i-TLE)
Particle concentration (size range >7 nm (D_p50), and the maximum detectable particle size > 3 μm)	Condensation Particle Counter (CPC, TSI model 3756)
Particle concentration (> 5.4 nm D_p50)	Condensation Particle Counter (CPC, Airmodus model A20)
Particle activation size distribution between 1 and 4 nm.	An Airmodus Nanoparticle Diluter (AND, Airmodus Ltd.) and nano-Condensation Nucleus Counter (A11 nCNC, Airmodus Ltd.)
Black carbon concentration	Multi-Angle Absorption Photometer (MAAP, Thermo Electron Corporation, Model 5012)
Black carbon concentration	A dual spot aethalometer (AE33, Magee Scientific)
Alveolar lung deposited surface area (LDSA) concentration	Pegasor AQ™ Urban instrument (Pegasor Ltd.)

Particle size distribution (size range **:** 3–950 nm)	The Differential Mobility Particle Sizer (Vienna type Differential Mobility Analyser, DMA) and Airmodus A20 CPC)
Concentration of CO, CO_2, and CH_4	Gas analyser for CO, CO_2 and CH_4 (Picarro G2401, Picarro Inc.)
Samples for PAH analyses	Daily PM_{10} filter sampling
Samples for sugar anhydride analyses	PM_1 filter sampling (one or two samples per day)
Concentration of $PM_{2.5}$ and PM_{10}	Fidas 200 (Palas)
Nitrogen oxides (NO_x)	APNA 370 (Horiba)
Ozone (O_3)	APOA 370 (Horiba)
Carbon monoxide (CO)	APMA 360 (Horiba)
Carbon dioxide (SO_2)	LI-7000 (LICOR)
Particle scattering coefficient	Nephelometer (model 3610, TSI)

Table S3. Instruments at the UB Supersite (SMEAR III).

Mast (31 m, agl)	
Quantity	Instrument
Air temperature (4, 8, 16 and 31 m)	Platimun resistance thermometer (Pt-100)
Wind (4, 8, 16 and 31 m)	2D ultrasonic anemometer (Thies Clima 2.1x)
Global radiation (31 m)	Kipp and Zonen CNR1
Reflected global (31 m)	Kipp and Zonen CNR1
Longwave radiation in (31 m)	Kipp and Zonen CNR1
Longwave radiation out (31 m)	Kipp and Zonen CNR1
Photosynthetic Active Radiometer (PAR, 31 m)	Kipp and Zonen PAR lite
Reflected PAR (31 m)	Kipp and Zonen PAR lite
Flux of momentum and heat (Eddy Covariance, 31)	Ultrasonic anemometer (Metek USA-1)
Flux of CO_2 and H_2O (Eddy Covariance, 31)	High frequency gas analyser (Li-Cor 7500 & 7000, infra-red absorbtion)
Total number concentration flux of aerosol particles (Eddy Covariance)	Water Condesation Particle Counter (WCPC, TSI-3781)
(2-4 m agl)	
Particle size distribution (size range **:** 3–950 nm)	The Differential Mobility Particle Sizer (Hauke-type DMA, 10.9 cm+TSI 3025; Hauke-type DMA, 28 cm+TSI 3010)
Particle concentration (size range >7 nm (Dp50), and the maximum detectable particle size > 3 μm)	Condensation particle counter (CPC, TSI 3756)
Particle size distribution (size range: 0.5– 20 nm)	Aerodynamic particle sizer (APS, TSI 3321)
Particle size distribution (size range: 1.3-4.5 nm)	Nano Condensation Nucleus Counter System (Airmodus A11 nCNC)
Mobility distribution of ions (0.8–40 nm) and size distribution of particles (2–40 nm)	Neutral cluster and Air Ion Spectrometer (Airel Ltd)
Nitrogen oxides (NO_x)	Chemiluminescence + thermal converter (TEI42S)

Ozone (O_3)	IR-absorption photometer (TEI49)
Carbon monoxide (CO)	Non-dospersive infrared (NDIR) absorption (Horiba APMA 370)
Sulphur dioxide (SO2)	UV-flurescence (Horiba APSA 360)
$PM_{2.5}$ and PM_{10}	TEOM 1405 (Thermo Scientific)
Physicum roof (29 m agl)	
Wind	Cup anemometer (Vaisala WAA141)
Air temperature	Platimun resistance thermometer
Sea level pressure	Barometer (Vaisala HMP243)
Relative humidity	Platimun resistance thermometer + thin film polymer sensor (Vaisala DPA500)
Dew point temperature	Platimun resistance thermometer + thin film polymer sensor (Vaisala DPA500)
Precipitation	Weighting rain gauge (Ott Pluvio)
Global radiation	Kipp and Zonen CNR1
Reflected global	Kipp and Zonen CNR1
Longwave radiation in	Kipp and Zonen CNR1
Longwave radiation out	Kipp and Zonen CNR1
PAR	Kipp and Zonen PAR lite
Reflected PAR	Kipp and Zonen PAR lite
Visibility	PWD

Table S4. Average concentrations of measured components during the traffic (averages without episodes) dominated period on workdays and weekends and their averages during four different episodes at the UB Supersite. PN concentration at UB Supersite was measured using an ultrafine CPC (Dp > 2.5 nm).

Compound	**Traffic workdays**	**Traffic weekends**	**E1** 22.1.2022 15:00 23.1.2022 10:00	**E2** 31.1.2022 07:00 5.2.2022 16:00	**E3** 13.2.2022 12:00 17.2.2022 23:00
PN *(p cm^{-3})*	7403	5295	12063	13056	6991
LDSA *(μm^2 cm^{-3})*	3.8	3.5	13.0	13.7	9.8
$PM_{2.5}$ *(μg m^{-3})*	1.2	1.3	6.3	7.3	5.6
$PM_{2.5-10}$ *(μg m^{-3})*	1.8	1.9	1.2	3.0	3.1
NO *(μg m^{-3})*	1.5	1.3	b.d.l	10.5	2.7
NO_2 *(μg m^{-3})*	9.4	6.7	11.0	24.5	16.2
BC *(μg m^{-3})*	0.18	0.17	0.91	0.98	0.70
CO *(ppb)*	141	147	197	236	192
CO_2 *(ppm)*	427	428	433	443	432
CH_4 *(ppb)*	2014	2020	2049	2076	2055
O_3 *(μg m^{-3})*	59	64	57	29	51
Total particulate organics *(μg m^{-3})*	0.59	0.47	1.83	1.90	2.84
Sulphate *(μg m^{-3})*	0.24	0.30	1.21	1.62	1.01
Nitrate *(μg m^{-3})*	0.22	0.13	1.35	0.65	1.35
Ammonium *(μg m^{-3})*	0.24	0.27	0.88	0.71	0.83
Chloride *(μg m^{-3})*	0.03	0.03	0.05	0.02	0.12

17 **Table S5**. Filter steps of the PDA for the figure S17.

Filter step	**Parameter**	**Traffic Supersite**	**UB Supersite**
Deriative filter (IQR)	IQR factor	1.7	1.7
	Window size	24 h	24 h
Threshold filter	Upper threshold	10^4 cm^{-3}	10^4 cm^{-3}
	Lower threshold	60 cm^{-3}	60 cm^{-3}
Neighboring points filter	On/off	On	On
Median filter	Median time interval	30 min	30 min
	Median deviation factor	1.5	1.5
Sparse data filter	Sparse window	30	30
(no. of data points)	Sparse threshold	24	24

18 **Table S6.** Filter steps of the PDA for the Figure 7.

Filter step	**Parameter**	**Traffic Supersite**	**UB Supersite**
Deriative filter (IQR)	IQR factor	1.7	1.7
	Window size	24 h	24 h
Threshold filter	Upper threshold	30^5 cm^{-3}	30^5 cm^{-3}
	Lower threshold	60 cm^{-3}	60 cm^{-3}
Neighboring points filter	On/off	On	On
Median filter	Median time interval	30 min	30 min
	Median deviation factor	1.5	1.5
Sparse data filter	Sparse window	30	30
(no. of data points)	Sparse threshold	24	24

19

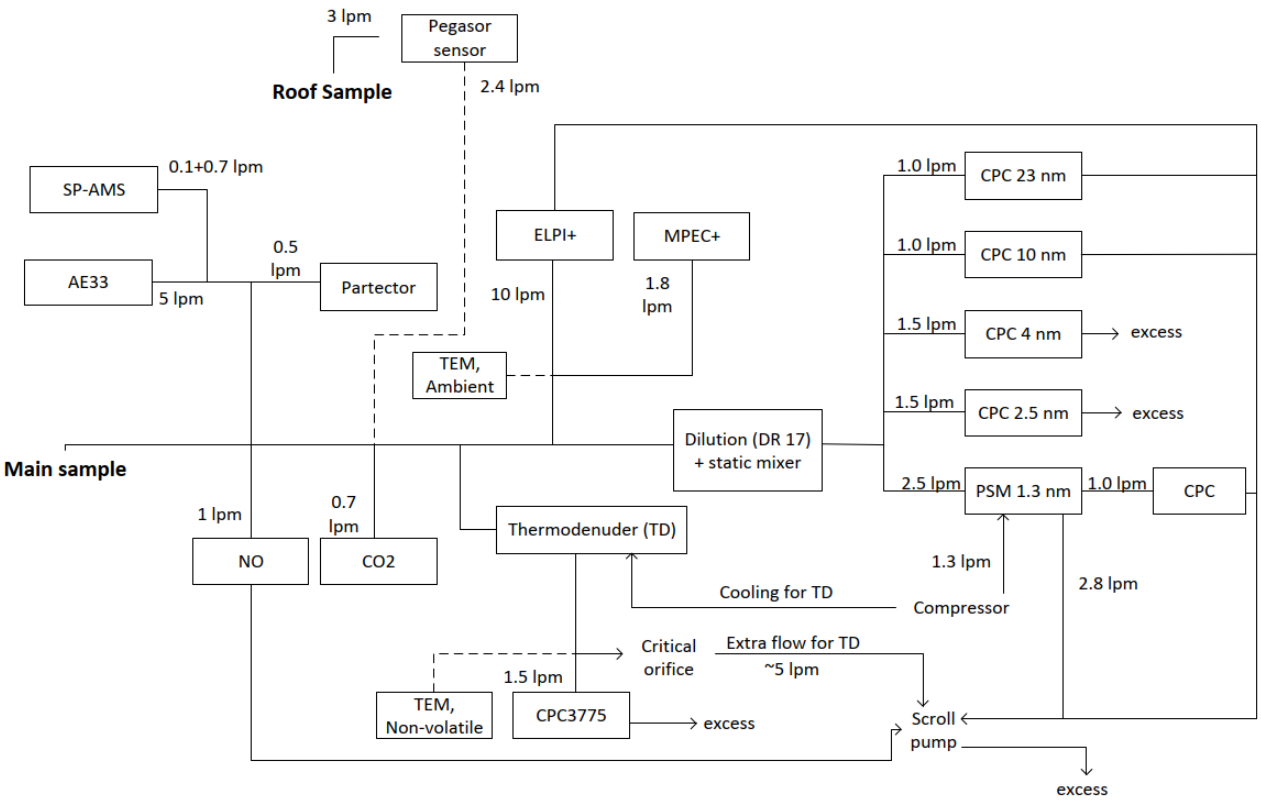

Figure S1. Measurement setup inside the Aerosol and Trace-gas mobile laboratory.

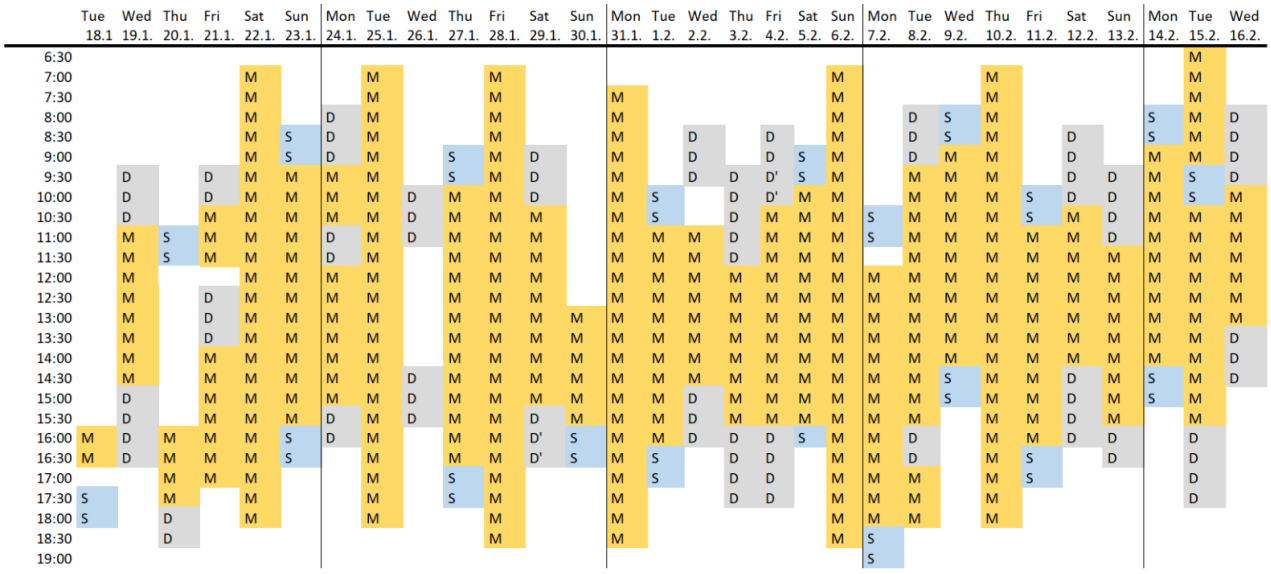

Figure S2. The measurement timeline of the Aerosol and Trace-gas mobile laboratory. Measurement activity is denoted with letters M (main street/Traffic Supersite), S (side street), D (driving), and D' (driving only along main street).

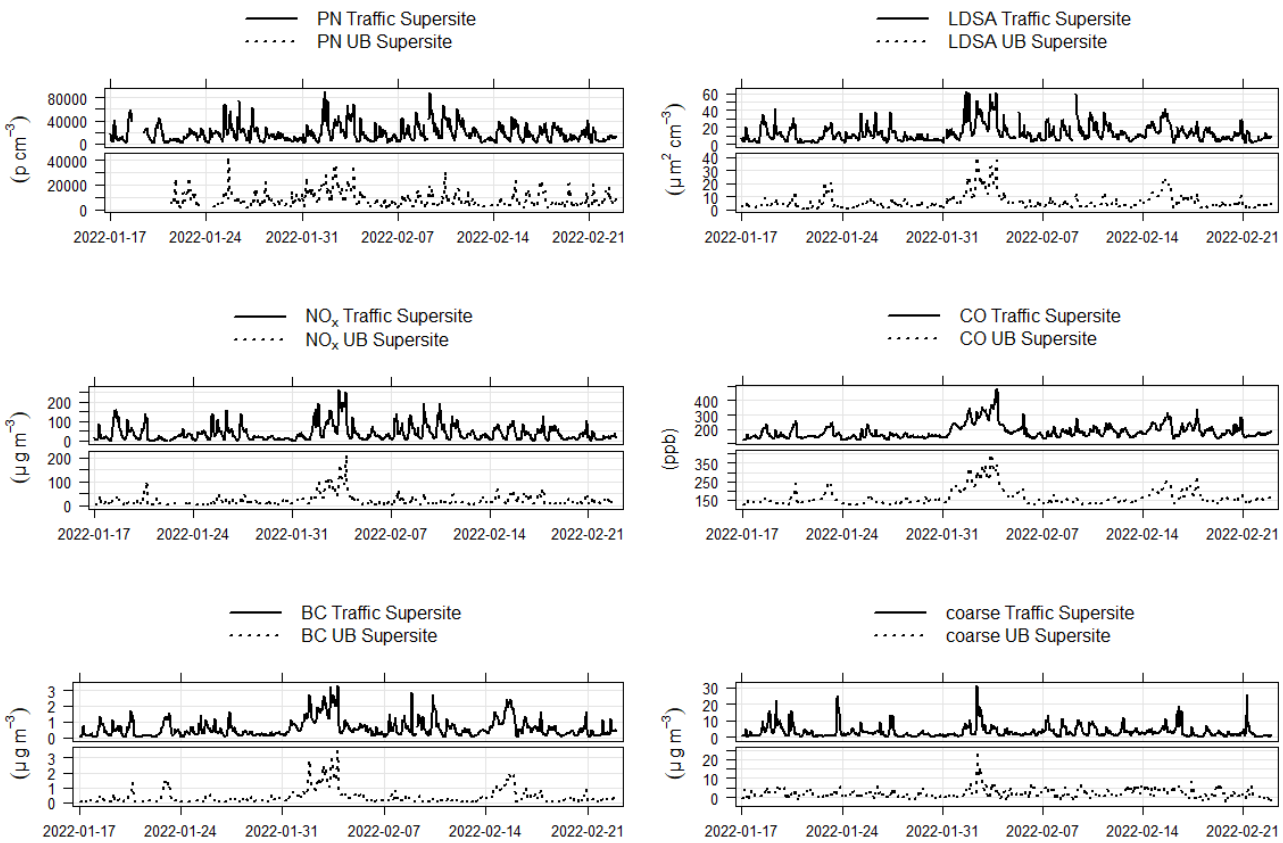

Figure S3. Time series of PN, LDSA, NO_x, CO, BC and $PM_{2.5-10}$ at the Traffic Supersite and at the UB Supersite during the measurement period. The cut size of the CPC at the Traffic Supersite is 5.4 nm and at the UB Supersite 7 nm.

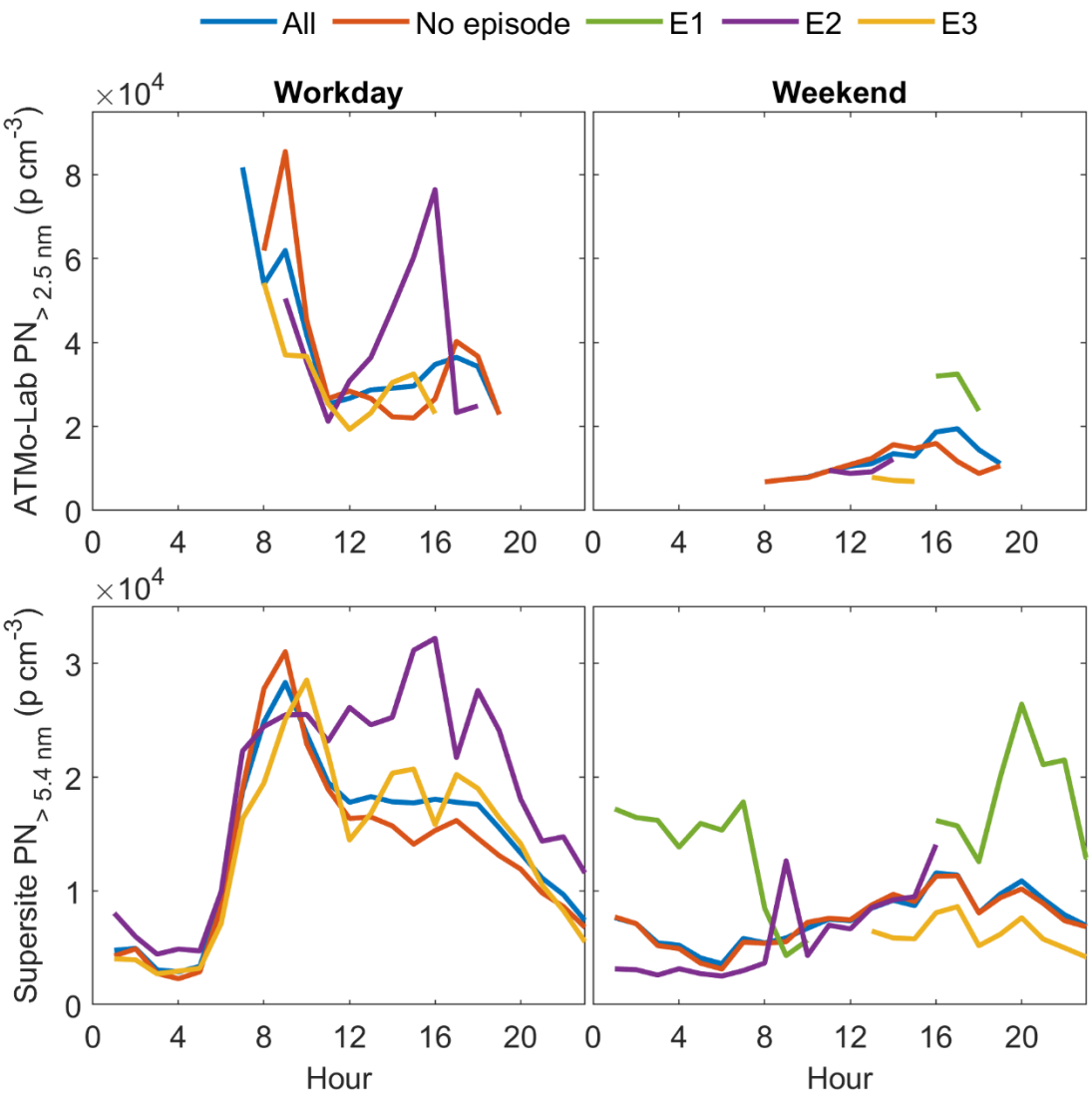

Figure S4. Diurnal variation of particle number concentration measured at the main street by an ATMo-Lab CPC (Dp_{50}: 2.5 nm) and at the Traffic Supersite CPC (Dp_{50}: 5.4 nm) on workdays and on weekends. Different episode time periods are denoted by the label. Geometric mean is used for averaging. Note that the ATMo-Lab did not measure continuously next to the Supersite as it was also utilised in driving measurements during the measurement days. Also, the ATMo-Lab measured during a shorter period between 18 January to 16 February 2022. Diurnal variation hours consisting of less than 30 minutes of measurement data were discarded.

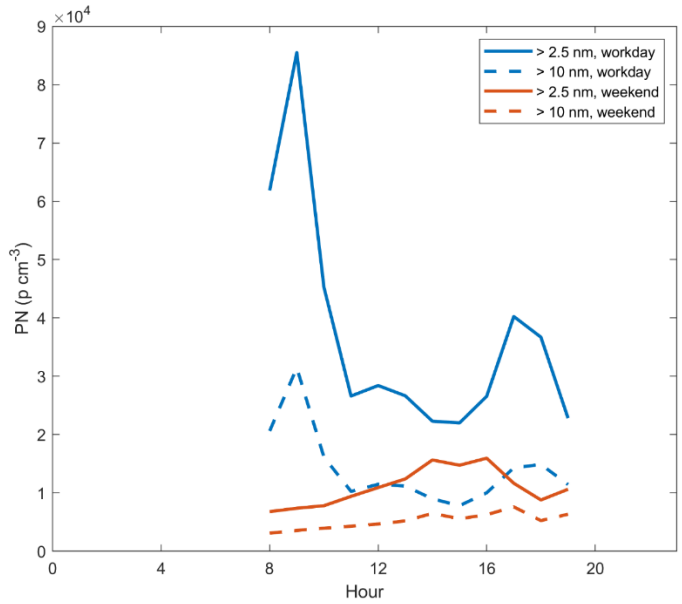

Figure S5. Diurnal variation of particle number concentration measured at the main street by ATMo-Lab on workdays and on weekends. Cut-off sizes (Dp_{50}: 2.5 nm and 10 nm) of the used instruments are indicated by the legend. Episode times are excluded from the data and geometric mean is used for averaging. Diurnal variation hours consisting of less than 30 minutes of measurement data were discarded.

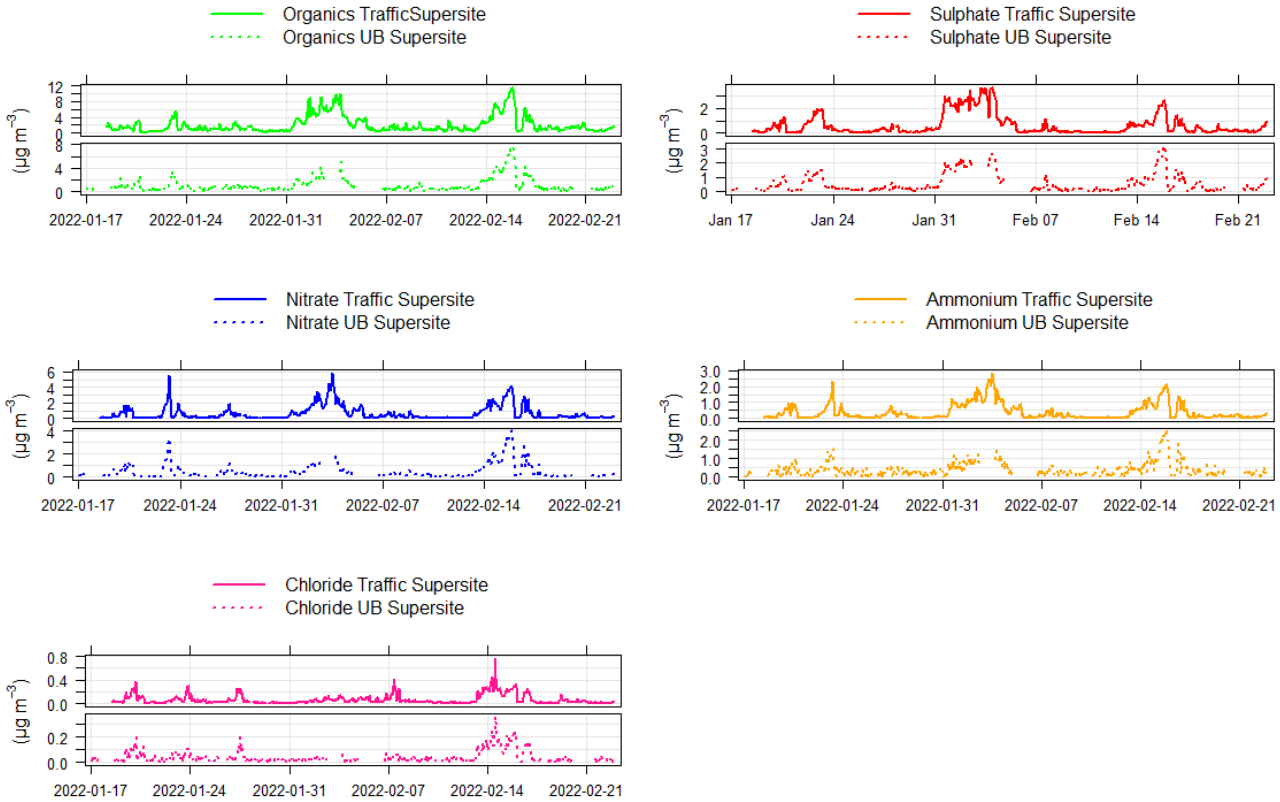

Figure S6. Time series of organics, sulphate, nitrate, ammonium and chloride at the Traffic Supersite and at the UB Supersite during the measurement period.

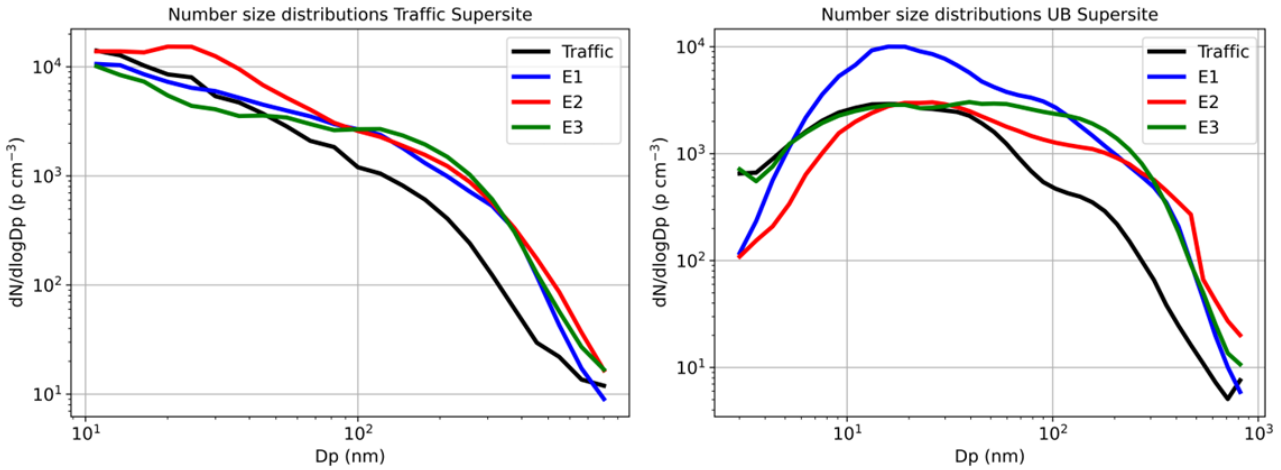

Figure S7. Average particle number size distributions measured with DMPS at the Traffic Supersite and at the UB Supersite stations during non-episodic situation and during the three episodes.

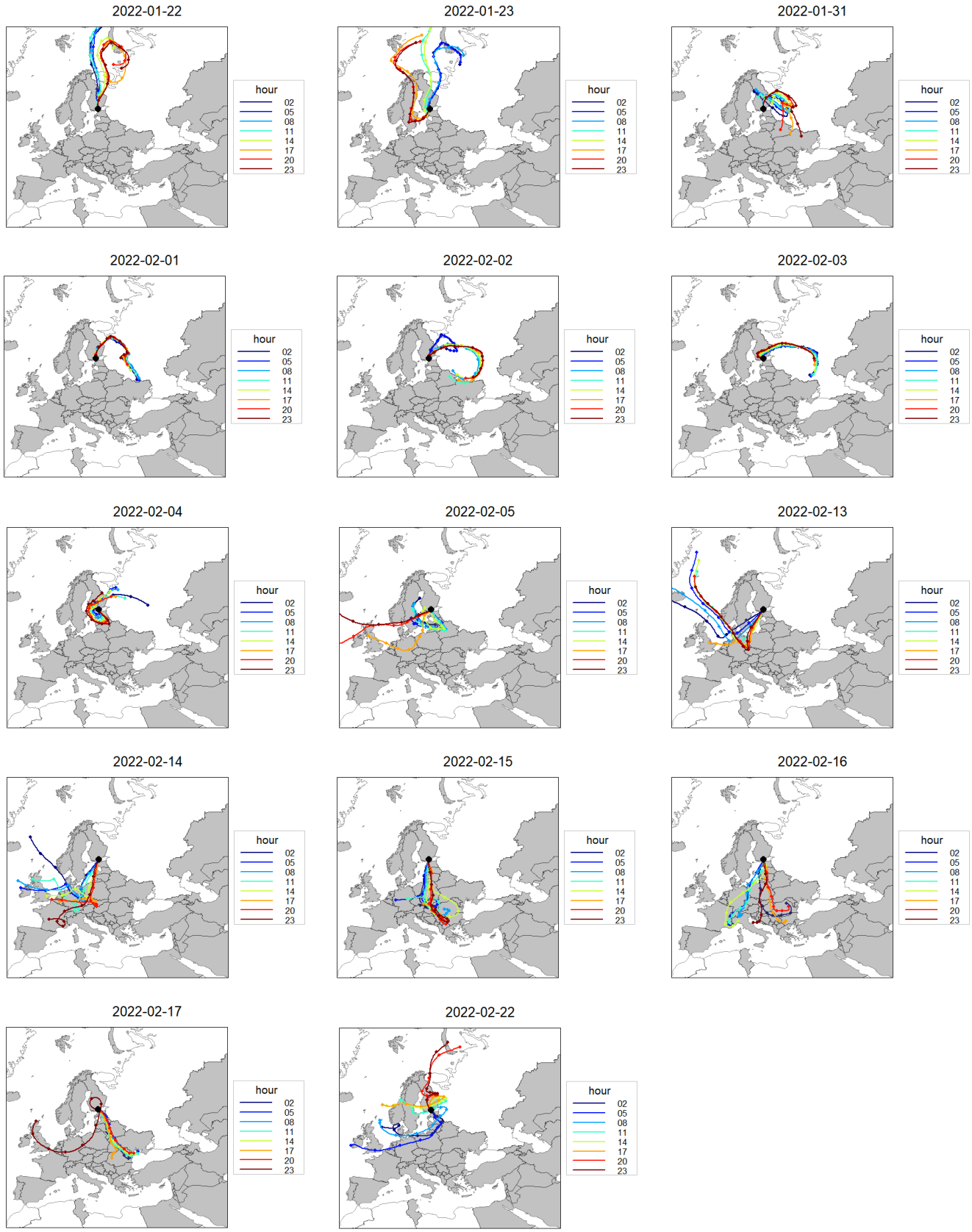

Figure S8. Daily 4-hour back trajectories during the episodes (local time).

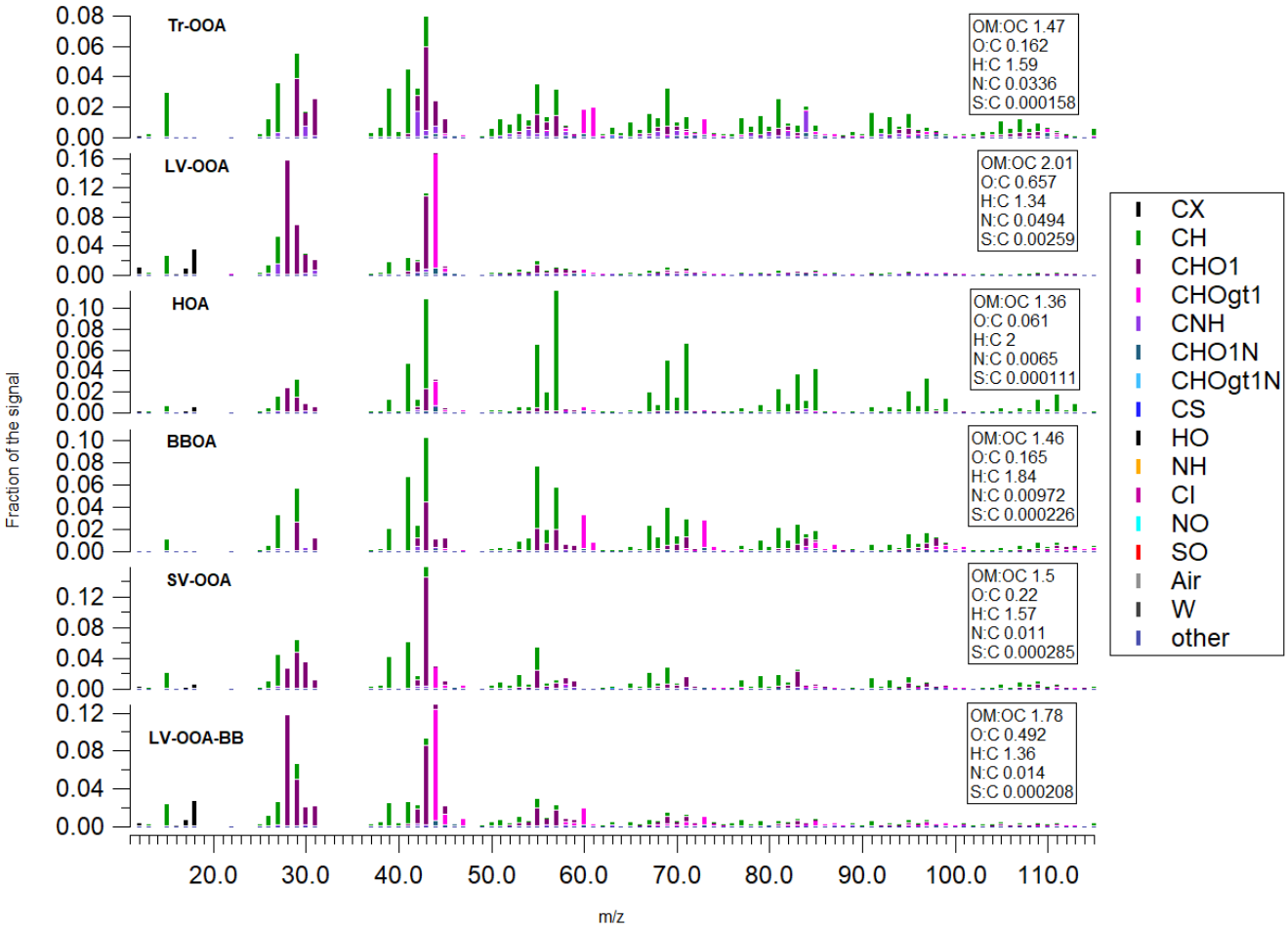

Figure S9. Mass spectra of the six factors obtained from PMF analysis.

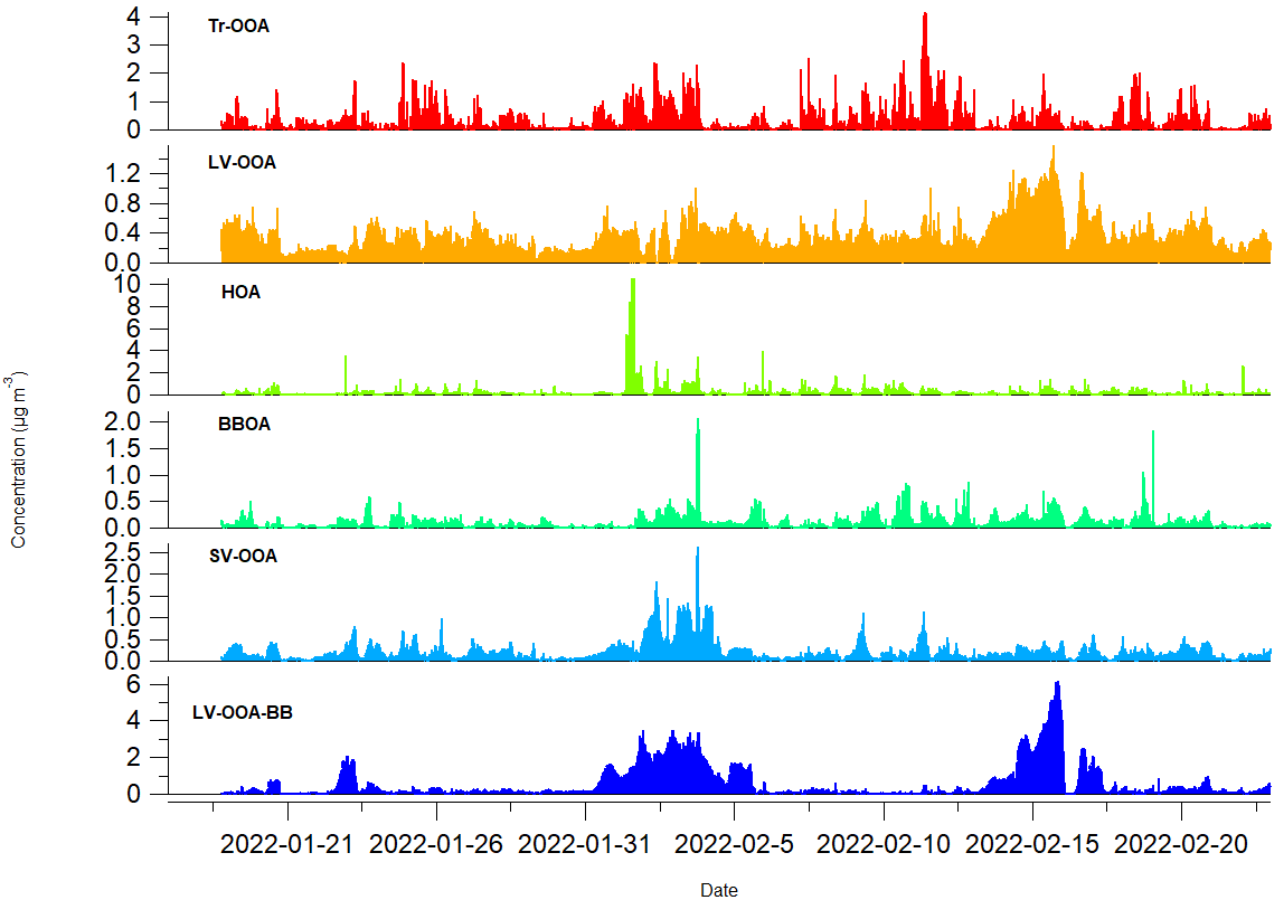

Figure S10. Time series of the six factors obtained from PMF analysis.

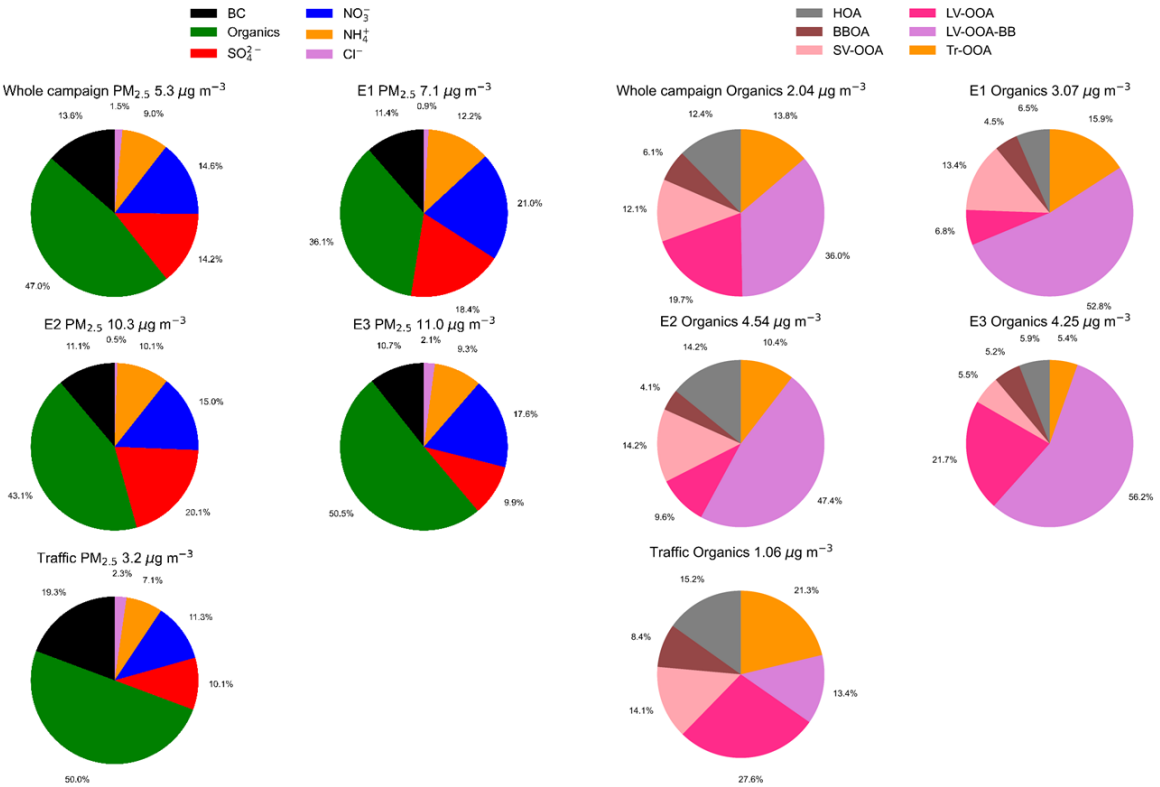

Figure S11. Pies showing the relative abundances of measured chemical components (left) and relative abundances of calculated organic fractions (right) during the whole campaign, during the three episodes (E1–E3) and during the traffic related time (non-episodes) at the Traffic Supersite.

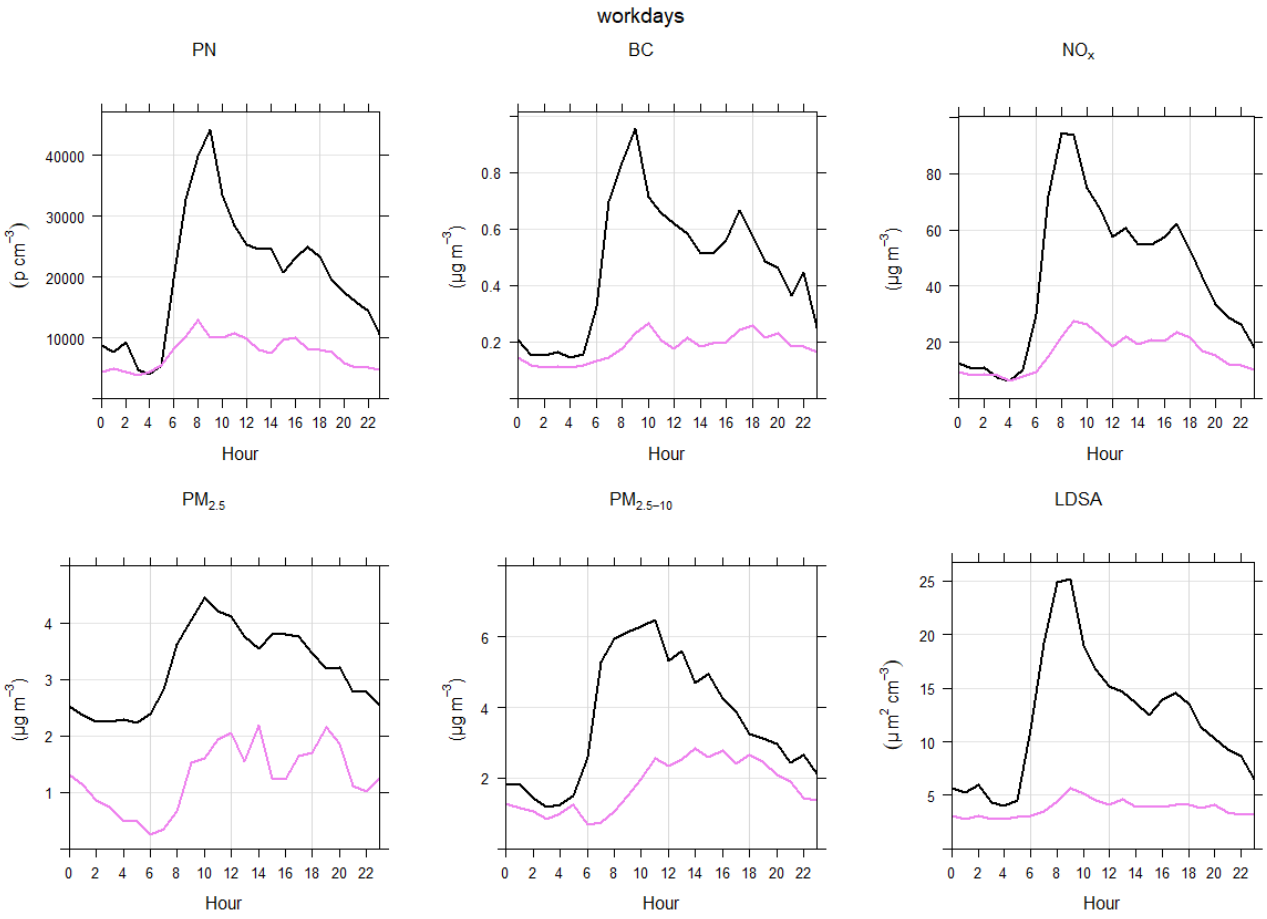

Figure S12. Hourly diurnal variations of concentrations of PN, BC, NO_x, $PM_{2.5}$, $PM_{2.5-10}$, and LDSA without episodes during workdays at the Traffic Supersite (black) and at the UB Supersite (violet) stations.

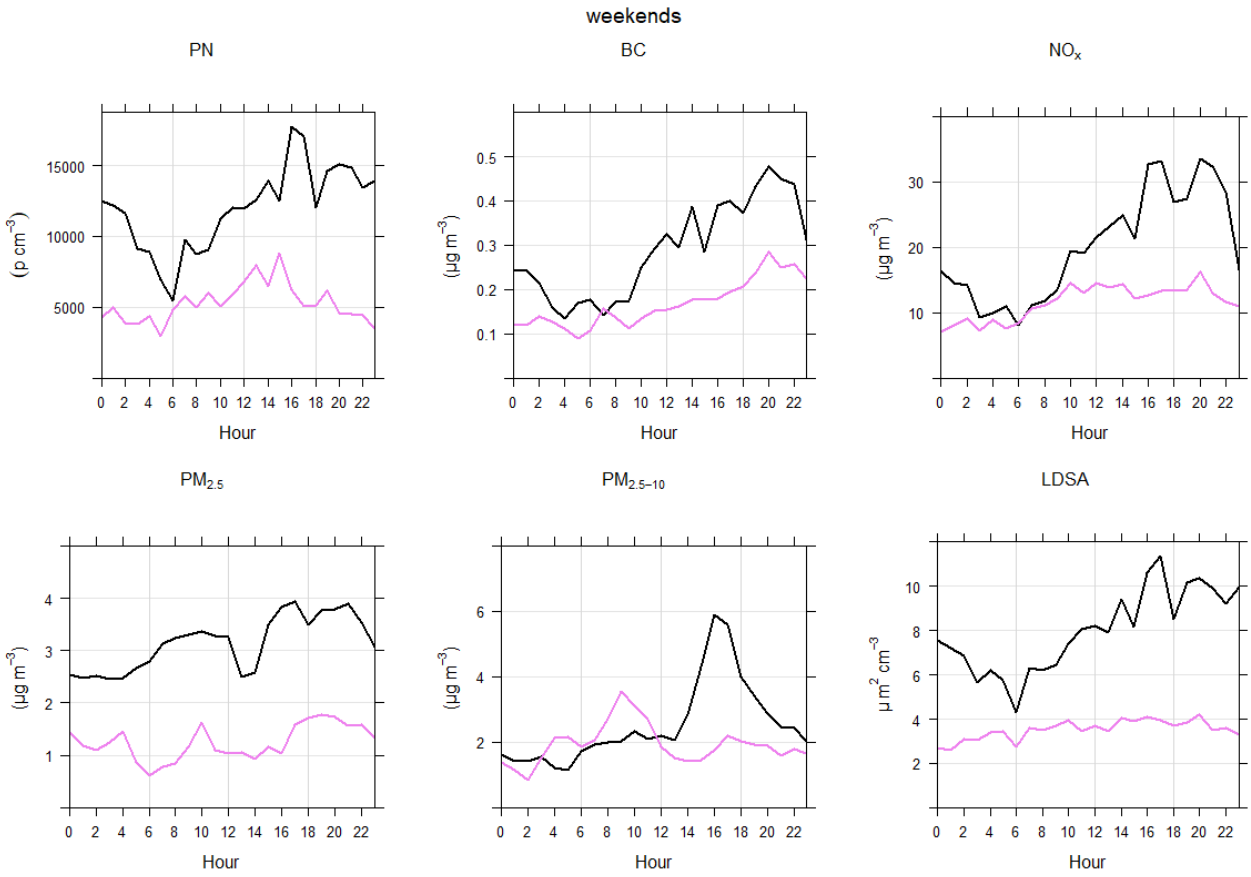

Figure S13. Hourly diurnal variations of concentrations of PN, BC, NO_x, $PM_{2.5}$, $PM_{2.5-10}$, and LDSA without episodes during weekends at the Traffic Supersite (black) and at the UB Supersite (violet) stations.

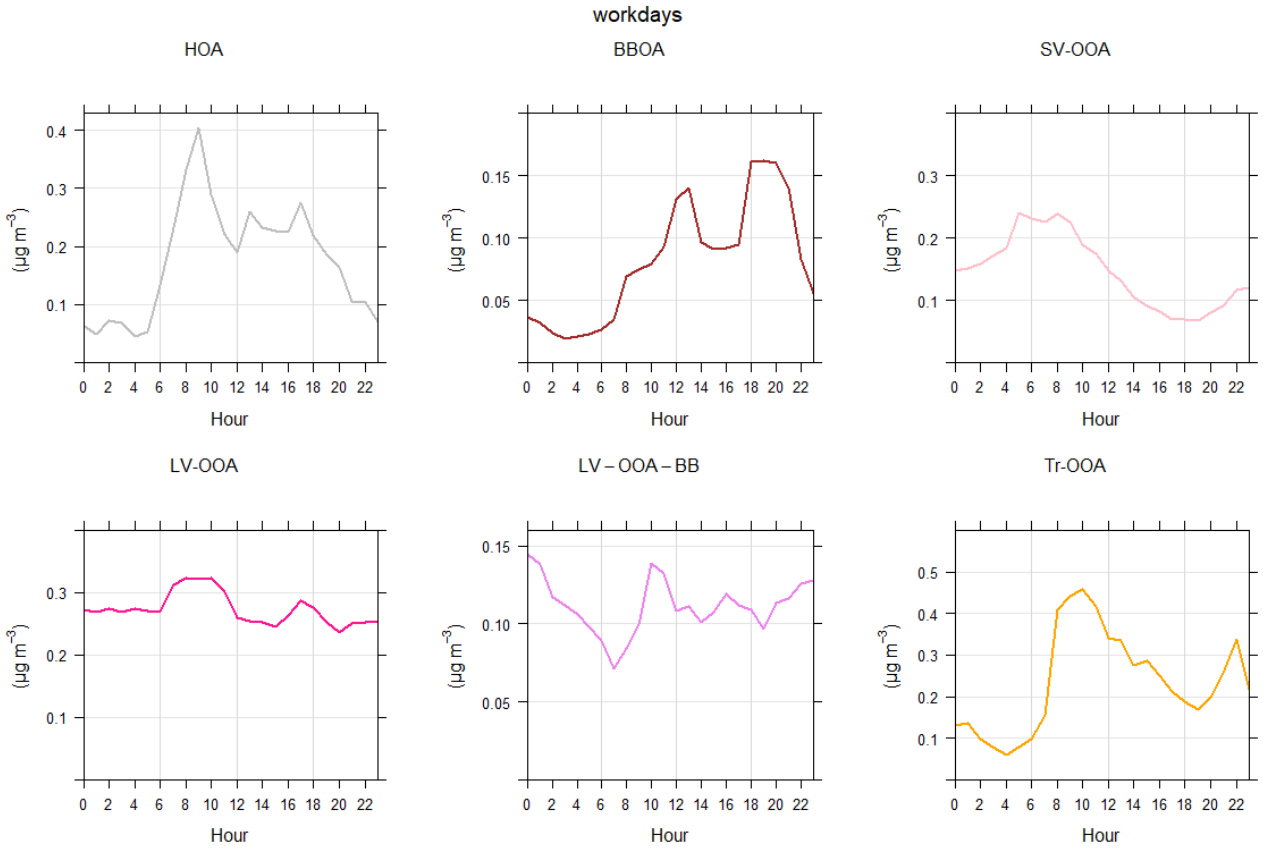

Figure S14. Hourly diurnal variations of concentrations of calculated organic fractions HOA, BBOA, SV-OOA, LV-OOA, LV-OOA-BB, and Tr-OOA without episodes at the Traffic Supersite during workdays.

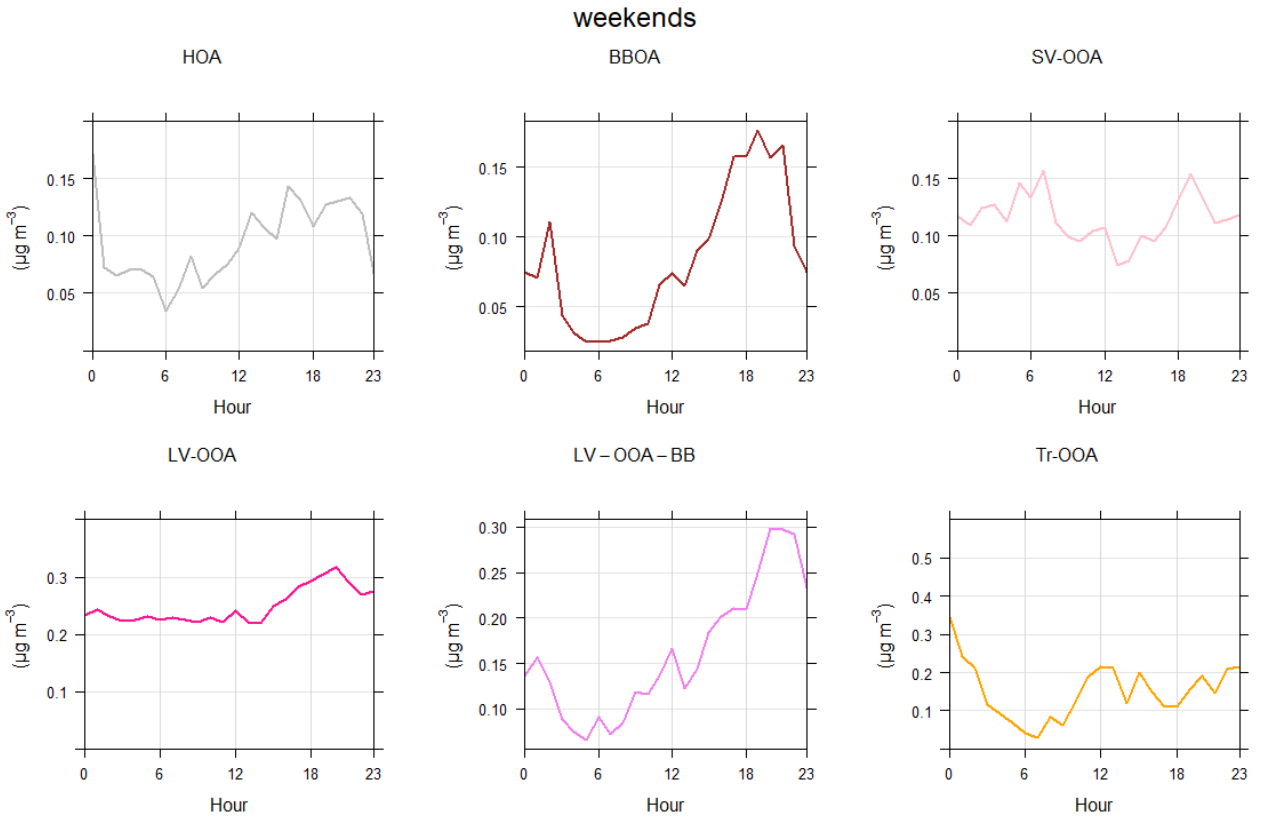

Figure S15. Hourly diurnal variations of concentrations of calculated organic fractions HOA, BBOA, SV-OOA, LV-OOA LV-OOA-BB, and Tr-OOA without episodes at the Traffic Supersite during weekends.

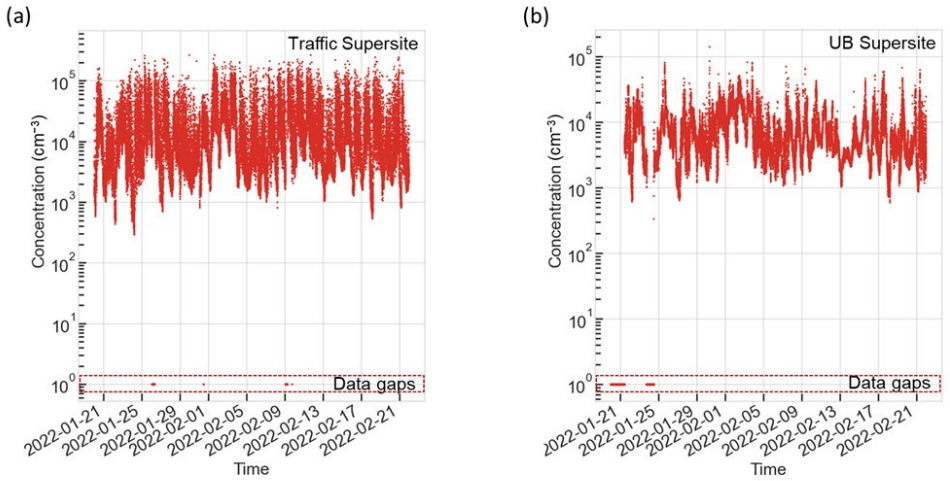

Figure S16. (a) CPC Traffic Supersite, 1 min resolution. (b) CPC UB Supersite, 1 min resolution. Data gaps (assigned to one) are shown in the bottom.

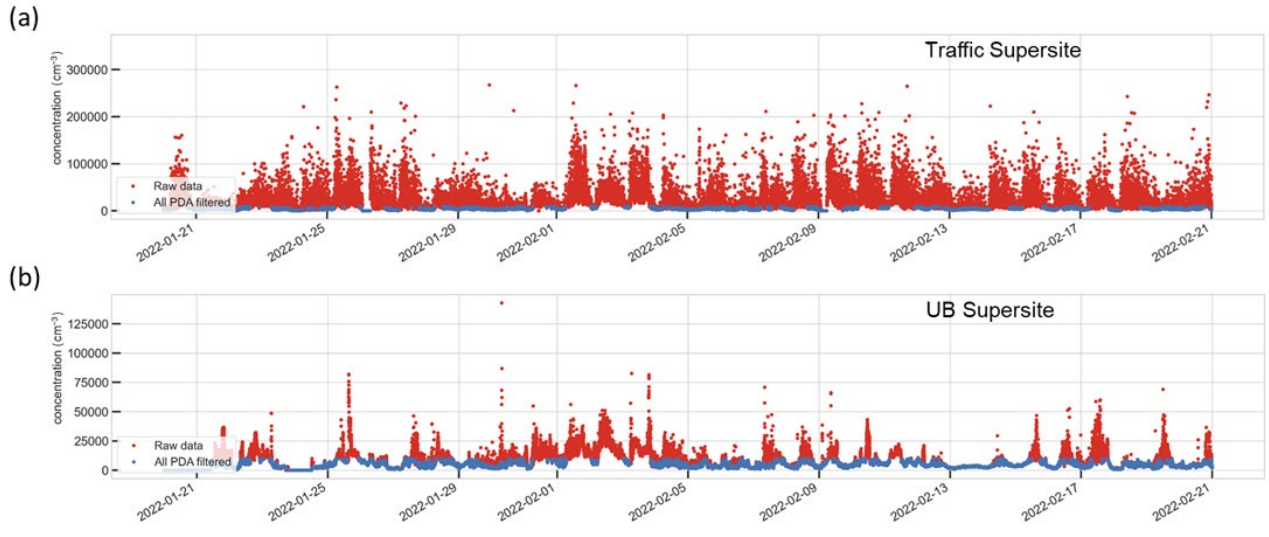

Figure S17. PDA filter results for the Traffic Supersite (a) and the UB Supersite (b). IQR derivative filter, upper threshold 10 000 cm^{-3}. See Table S

The meteorological preprocessor MPP-FMI

The meteorological pre-processing model of the Finnish Meteorological Institute (MPP-FMI) is based on the method of van Ulden and Holtslag (1985), in which the parameterization of boundary layer is evaluated with energy budget method using synoptic weather observations and meteorological sounding data as input. A brief overview of the method is given in the following, based on detailed descriptions of the method in Karppinen et al. (1997, 1998, 2000), and Backman et al. (2017).

Evaluation of scaling parameters u_*, θ_* and L

The main boundary layer parameters include friction velocity (u_*), temperature scale for turbulent heat transfer (θ_*), and Monin Obukhov length (L), which are evaluated from synoptic weather observations. In addition, potential temperature profiles from meteorological soundings are used for estimating the mixing height.

According to surface-layer similarity theory, friction velocity (u_*) is related to vertical profile of wind speed:

$$u_* = \frac{U(z)k}{ln\left(\frac{z}{z_0}\right) - \psi_m\left(\frac{z}{L}\right) + \psi_m\left(\frac{z_0}{L}\right)} \ , \qquad (1)$$

where U(z) is wind speed at height z, z_0 is the roughness length, and k is the von Karman constant. The stability functions ψ_m used are

$\psi_m = (1 - 16z/L)^{1/4} - 1$ for L < 0, and

$\psi_m = -17\left(1 - e^{-0.29z/L}\right)$ for L > 0. (2)

The temperature scale for turbulent heat transfer (θ_*) is a function of the turbulent heat flux at the ground surface (H_o) and the friction velocity:

$$\theta_* = -\frac{H_o}{\varrho_a c_p u_*} \ , \quad (3)$$

where ρ_a is the density of air, and c_p is the specific heat capacity of air. Temperature scale can also be presented as

$$\theta_* = \frac{k[\theta(z_2) - \theta(z_1)]}{ln\left(\frac{z_2}{z_1}\right) - \psi_h\left(\frac{z_2}{L}\right) + \psi_h\left(\frac{z_1}{L}\right)} \ , (4)$$

where z_1 and z_2 are arbitrary heights in the surface layer, θ is the potential temperature, and ψ_h are the stability functions for heat:

$\psi_h = 2ln\left(\frac{1+y^2}{2}\right)$, where $y = (1 - 16z/L)^{1/4}$ for L < 0, and

$\psi_h = -5z/L$ for L > 0. (5)

The Monin-Obukhov length is defined as

$$L = \frac{T_2 u_*^2}{kg\theta_*} , \qquad (6)$$

where T_2 is the air temperature at the height of 2 m, k is the von Karman constant, and g is the acceleration of gravity.

The energy budget at the ground surface in a stationary and horizontally homogeneous boundary layer can be presented as

$$H_o + \lambda E_o = Q^* - G \ , \qquad (7)$$

where λE_o is the latent heat flux, Q* is the net radiation flux, and G is the conductive heat flux to the ground. The net radiation flux can be written as

$$Q^* = Q_i^* + \Delta Q^* \ , \qquad (8)$$

where Q_i^* is the radiation flux in an isothermal atmosphere, and ΔQ^* is the deviation from this in the real atmosphere, evaluated as

$$\Delta Q^* = 4\sigma T_r^3 (T_r - T_0) \ , \qquad (9)$$

where T_r is the air temperature at reference height of 50 m, T_0 is the surface radiative temperature, and σ the Stefan-Boltzmann constant. Q_i^* can be expressed as the sum of net shortwave radiation (K^*), net longwave radiation (L_{net}) and longwave radiation from clouds (L_c):

$$Q_i^* = K^* + L_{net} + L_c \quad . (10)$$

The estimation of latent heat flux is based on Penman-Monteith equation

$$\lambda E_o = \alpha \left[\frac{S}{S+1}(Q^* - G) + \varrho_a c_p u_* \theta_d\right] . \qquad (11)$$

where α is the Priestley-Taylor parameter ($0.5 \leq \alpha \leq 1.0$), θ_d an empirical temperature scale (0.033 K), and S is the slope of saturation enthalpy curve. The Priestley-Taylor parameter is estimated from solar elevation angle, precipitation, temperature and snow depth.

Combining equation (11) with wind profile equation (1) and the definition of L in equation (6), the temperature scale can be presented as

$$\theta_* = \left(\frac{\alpha S}{S+1} - 1\right)\left[\frac{Q^* - G}{\varrho_a c_p u_*}\right] - \alpha\theta_d \; . \qquad (12)$$

The radiation fluxes in equation (7) are presented in terms of measured meteorological parameters. The parameterization is mostly based on van Ulden and Holtslag (1985), complemented with parameterizations based on experimental data from Jokioinen observatory in southern Finland, as described in Karppinen et al. (1997, 1998). The net shortwave radiation is computed from surface albedo and measured incoming radiation, and the net longwave radiation is a function of surface radiative temperature. The radiation from clouds is evaluated using the observed amount of low and mid-level clouds, and cloud base temperature, which is computed using adiabatic temperature profile and observed cloud base height, and taking into account the seasonal variation of albedo with empirical regression equations based on data from Jokioinen. Ground heat flux can be presented as

$$G = -A_G(T_r - T_0) \; , \qquad (13)$$

where A_G is an empirical constant (5 $Wm^{-2}K^{-1}$). The surface radiative temperature is not observed directly. The temperature difference can, however, be eliminated (van Ulden and Holtslag, 1985). For unstable boundary layer, equations (8) and (9) are combined with equation (13), and ΔQ^* is presented as $\Delta Q^* = -A_H Q^*$, where A_H is an empirical coefficient. For stable boundary layer, equations (8), (9) and (13) are combined and temperature difference is presented using potential temperature profile equation

$$T_r - T_0 = \theta_* \left(30 + \frac{z_r}{kL}\right) - \Gamma_d z_r \; , \qquad (14)$$

where z_r = 50 m and Γ_d is the dry adiabatic lapse rate (0.01 Km^{-1}). The scaling parameters u_*, θ_* and L are solved with an iterative procedure by varying L and using both equation (12) and profile equation (4).

Evaluation of mixing height in winter

The method of generating the hourly time series of mixing heights is different for winter and summer periods. As this study concerns only the winter season, the method for winter is described in detail in the following.

Evaluation of mixing height is based on routine midday (12 UTC) and midnight (00 UTC) sounding data. In winter, the boundary layer is mostly stable or near neutral in Finland. The mixing height h at time t is expressed in terms of friction velocity u_*:

$$h(t) = s(t)u_*(t) \, , \qquad (15)$$

where s is the linear interpolation coefficient, applied to compute the mixing heights between two consecutive soundings, e.g., the coefficient for hours between 00 and 12 UTC is

$$s(t) = s(00) + (s(12) - s(00))\frac{t}{12} . \qquad (16)$$

The parameter s at midday and midnight is computed from corresponding mixing heights, which are evaluated by analyzing the vertical potential temperature profiles of soundings. The first two significant levels, i.e., levels for which the vertical profile of temperature direction differ significantly from a straight line, are selected from the sounding. The potential temperature gradient g_l is calculated between these levels:

$$g_1 = \frac{\theta_2 - \theta_1}{z_2 - z_1}, \quad (17)$$

where θ is the potential temperature and z is the corresponding height of the level.

If the first gradient is greater than 0.01, the mixing height is

$$h^* = \frac{4.5}{g_1 + 0.005} \quad . \quad (18)$$

If the gradient is between 0 and 0.01, a test temperature θ_h is calculated:

$$\theta_h = \theta_1 + g_1 h^*. \quad (19)$$

If the potential temperatures of the sounding do not exceed θ_h, h^* is the mixing height. If a significant level i with potential temperature above θ_h exists, the mixing height is linearly interpolated between the lowest such level and the previous significant level:

$$h = min\left[z_i^* + \frac{\theta_h - \theta_i^*}{\theta_i - \theta_i^*}(z_i - z_i^*), h^*\right], \quad (20)$$

where θ_i and θ_i^* are the potential temperatures of the level i and the previous significant level, and z_i and z_i^* are the corresponding heights of the level.

The simple dry parcel intersection method (Holzworth, 1964) is used to estimate the mixing height for unstable situations.

References

Backman, J., Wood, C.R., Auvinen, M., Kangas, L., Hannuniemi, H., Karppinen, A., and Kukkonen, J.: Sensitivity analysis of the meteorological preprocessor MPP-FMI 3.0 using algorithmic differentiation, Geosci. Model Dev., 10, 3793-3803, 2017.

Holzworth, G.C.: Estimates of mean maximum mixing depths in the contiguous United States, Monthly Weather Review, 92, 235-242, 1964.

Karppinen, A., Joffre, S. M., and Vaajama, P.: Boundary-layer parameterization for Finnish regulatory dispersion models, Int. J. Environ. Pollut., 8, 557–564, 1997.

Karppinen, A., Kukkonen, J., Nordlund, G., Rantakrans, E., and Valkama, I.: A dispersion modelling system for urban air pollution. Publications on Air Quality No. 28, Finnish Meteorological Institute, 1998.

Karppinen, A., Joffre, S. M., and Kukkonen, J.: The refinement of a meteorological preprocessor for the urban environment, Int. J. Environ. Pollut., 14, 565–572, 2000.

van Ulden, A.P. and Holtslag, A.A.M.: Estimation of Atmospheric Boundary Layer Parameters for Diffusion Applications, J. Clim. Appl. Meteorol., 24, 1196–1207, 1985.